Materials Horizons

ROYAL SOCIETY OF CHEMISTRY

COMMUNICATION

View Article Online
View Journal



Cite this: DOI: 10.1039/d6mh00613b

Received 30th March 2026,
Accepted 21st April 2026

DOI: 10.1039/d6mh00613b

rsc.li/materials-horizons

# Candidate electro-optic molecular crystals for future optoelectronic integration

Keishi Sunami, *[a] Sachio Horiuchi, [a] Yoriko Sonoda, [a] Naomi Fujiki,[a] Toshiki Higashino, [a] Yuki Atsumi, [b] Shoji Ishibashi [a] and Jun'ya Tsutsumi *[a]

**The rapid advancement of communication technology necessitates the development of hybrid optical modulators that integrate silicon photonics with electro-optic (EO) materials to enable ultrafast, low-power, and compact photonic devices. However, no existing material simultaneously meets the requirements for high EO performance, process compatibility, and thermal stability, which are essential for practical optoelectronic integration. Here, we present 4-(4′-nitrophenylazo)diphenylamine (NDPA) and its derivative, novel nonlinear optical molecular crystals discovered through materials screening incorporating crystal habit prediction. They demonstrate crystallization into high-quality aligned thin films and ultrafine silicon slot fillings through the capillary action of melts. The resulting EO performance much exceeds that of conventional lithium niobate, with excellent thermal stability maintained for over 1000 hours at 393 K. The present EO materials satisfying all the requirements above are promising candidates for silicon-organic hybrid optical modulators, opening a significant step toward scalable and high-performance optoelectronic technologies.**

### New concepts

This study presents a new strategy for EO material design suitable for optoelectronic integration: melt-casting molecular crystalline thin films. Molecular crystals have long been studied for their excellent nonlinear optical activity but dismissed for optoelectronic integration due to poor film formability, which is essential for device fabrication. Here, we break through this limitation by exploring novel EO molecular crystals through materials screening that incorporates crystal habit prediction with two-dimensional crystal growth. Crucially, the materials identified in this study form high-quality aligned thin films by melt casting, enabling filling of sub-micron silicon slots. Moreover, unlike conventional lithium niobate, which requires complex integration processing, and EO polymers, which suffer from poor thermal stability, the presented molecular crystals combine high EO performance, scalable processability, and thermal stability; they overcome all the major drawbacks of existing EO materials. Thus, by challenging the prevailing notion that molecular crystals are incompatible with optoelectronic integration, the present study establishes a new paradigm in EO material design and highlights EO molecular crystals as practical candidates for next-generation optoelectronic devices such as high-speed optical modulators, optical phased arrays, and spatial light modulators.



## 1 Introduction

A massive increase of connected devices and a rapid advancement of artificial intelligence cause a significant rise in data traffic, making high-speed and energy-efficient data communication an urgent challenge. The promising solution is optoelectronic integration to combine optical communication with electronic data processing within a silicon chip or a silicon package.[1,2] This concept relies on silicon photonics technologies which allow fabricating optical circuits on silicon chips.[3–5] Among the technologies, an on-chip optical modulator plays a vital role on electrical-to-optical signal conversion. Since conventional on-chip optical modulators, exploiting the free-carrier plasma dispersion effect of silicon,[6,7] are approaching their performance limit, there is a strong demand to transition toward modulators based on the high-speed and energy-efficient electro-optic (EO) effect. However, silicon lacks the Pockels effect, *i.e.* EO-inactive, so that considerable research efforts have been directed to integrate EO-active materials onto silicon waveguides.[8,9]

Requirements of EO materials toward the optoelectronic integration are not only excellent EO activity but also CMOS-process compatibility and high thermal stability.[2] Excellent EO activity is essential to miniaturize optical modulators toward scalable photonic integrated circuits. CMOS-process compatibility is critical for mass production in semiconductor foundries, while high thermal stability is indispensable for integrating optical modulators with heat-generating electronic circuits. One of the promising candidates is lithium niobate (LN). It is

[a] *Core Electronics Technology Research Institute (CETRI), National Institute of Advanced Industrial Science and Technology (AIST), Tsukuba, Ibaraki 305-8565, Japan. E-mail: k.sunami@aist.go.jp, junya.tsutsumi@aist.go.jp*
[b] *Photonics-Electronics Integration Research Center (PEIRC), National Institute of Advanced Industrial Science and Technology (AIST), Tsukuba, Ibaraki 305-8568, Japan*

a well-established EO material with low optical loss and high thermal stability and can be integrated into silicon through transferring and low-temperature bonding of lithium niobate on insulator (LNOI).[8,10] Nevertheless, several challenges remain, including limited process yield due to alignment tolerances and bonding interface quality, as well as the overall complexity of the integration process. Another candidate is an EO polymer which recently attracts attention as a new class of EO materials.[11–15] It has EO activity much higher than the lithium niobate and can be easily deposited on silicon waveguide through solution process. Furthermore, by combining with a slot waveguide structure,[16] it allows highly efficient optical modulation, enabling significant miniaturization of optical modulators. However, it requires high electric-field poling to align chromophores and inherently suffers from thermal instability due to orientational relaxation of the aligned chromophores. To improve thermal instability, there have been efforts such as elevating glass transition temperature and crosslinking polymer backbone,[17,18] whereas they introduce trade-offs: the former reduces poling efficiency, while the latter degrades optical transparency due to increased light scattering.

EO molecular crystals, exemplified by 4-dimethylamino-*N*-methyl-4-stilbazolium tosylate (DAST)[19–21] and 2-(3-(4-hydroxystyryl)-5,5-dimethylcyclohex-2-enylidene) malononitrile (OH1),[22–24] exhibit nonlinear optical (NLO) activity as high as EO polymers, so that they have been utilized especially for terahertz photonics applications.[24] As they are crystalline materials whose chromophores spontaneously align without poling, they are inherently free from thermal instability caused by orientational relaxation in sharp contrast to EO polymers. Despite these advantages, their application has been limited to discrete optical components. The main reason not to be applied to photonic integrated circuits is poor film formability due to their anisotropic crystal growth although there are a few exceptions such as *N*-benzyl-2-methyl-4-nitroaniline (BNA).[25–27]

Here we report novel EO molecular crystals that excel in all of EO activity, film formability, and thermal stability. Systematic materials screening was conducted on the Cambridge structural database (CSD) with introducing parameters such as hyperpolarizability, crystal habit, and melting point which are relevant to EO activity, film formability, and thermal stability, respectively. Then, 8 kinds of extracted EO molecular crystals were applied for melt-casting experiments to examine their film formability. Consequently, two materials were found to exhibit excellent film formability due to two-dimensional crystal growth: 4-((4-nitrobenzylidene)amino)-*N*-phenylaniline (PNPA) and 4-(4′-nitrophenylazo)-diphenylamine (NDPA). Remarkably, their EO activities surpassed conventional LN and were stable over 1000 h under high temperature condition of 393 K. These properties highlight their potential as next-generation EO materials for integrated photonics.

## 2 Results and discussion

### 2.1 Materials screening by crystal habit prediction

Conventional materials screening for EO materials has employed only two parameters with no exception, *i.e.* molecular hyperpolarizability $\beta$ and molecular orientation within a crystal. This is reasonable to find high EO-performance materials because highly oriented chromophores with large hyperpolarizability result in superior EO activity. For example, molecular design for enlarging $\beta$ is to attach strong electron donating and accepting substituents at both terminal of extended π-conjugation backbone,[28,29] as exemplified by the materials displayed in Fig. 2 and Fig. S1 and Table 1. However, such a screening alone is not sufficient for high film formability and thermal stability that are required toward optoelectronic integration of the EO materials. Therefore, the materials screening in this study introduced a crystal-habit parameter $I_{2D}$ and a melting point $T_m$ which are indicators for the film formability and the thermal stability, respectively. $I_{2D}$ was obtained as follows: crystal habit was simulated for various molecular crystals recorded in CSD by the surface attachment energy calculation program, HABIT,[30,31] with the Gavezzotti's empirical force field.[32,33] Then, its anisotropy estimated by ellipsoid fitting was plotted in a triangle graph as a function of $b/a$ and $c/a$ where each corner corresponds to 1-dimensional crystal growth ($b/a = c/a = 0$), 2-dimensional crystal growth ($b/a = 1$, $c/a = 0$), and 3-dimensional crystal growth ($b/a = c/a = 1$), respectively (Fig. 1a). $I_{2D}$ was defined as the distance from the 2-dimensional crystal growth, so that high film formability is expected for small $I_{2D}$. Fig. 1b shows $T_m$ of EO molecular crystals plotted as a function of $I_{2D}$ with the $\beta_{tot}$ value (see Fig. 2 and Fig. S1 for the molecular structures). Each point corresponds to EO molecular crystals extracted from CSD that meet the following criteria: they consist of single component D–π–A chromophores where electron-donating (D) and electron-accepting (A) functional terminal groups are connected by π-conjugated bonds. Their total hyperpolarizability (non-resonant) $\beta_{tot}$ simulated by a quantum chemical calculation are as high as $50 \times 10^{-40}$–$520 \times 10^{-40}$ m$^4$ V$^{-1}$. Their angle $\theta$ between molecular hyperpolarizability vector and crystal polar axis ranges 0–30° so that their EO coefficients (second order NLO susceptibility) are nearly maximized along the crystal polar axis. Note that the diagonal tensor component of EO coefficient is proportional to $\cos^3\theta$, meaning large EO coefficient for small $\theta$. Among the materials plotted in Fig. 1b, the ones with small $I_{2D}$ are favorable

Table 1 Physical properties of EO molecular crystals. Molecular total hyperpolarizability (non-resonant) $\beta_{tot}$, absorption threshold wavelength $\lambda_{th}$, melting point $T_m$, and the difference between $T_m$ and the solidification point $T_s$ in the EO molecular crystals. $\beta_{tot}$ was calculated by Gaussian software. $\lambda_{th}$ was evaluated by the diffuse reflectance spectroscopy. $T_m$ and $T_s$ were determined by the DSC measurements (see Section 4). For DMACB, the value of $T_m - T_s$ was undefined due to the structural change after re-solidification (see SI)

| Material | $\beta_{tot}$ ($10^{-40}$ m$^4$ V$^{-1}$) | $\lambda_{th}$ (nm) | $T_m$ (K) | $T_m - T_s$ (K) |
|---|---|---|---|---|
| NDPA | 521.2 | 665 | 436 | 34 |
| PNPA | 416.7 | 629 | 452 | 75 |
| OH1 | 326.5 | 592 | 482 | >212 |
| CPNC | 270.9 | 565 | 470 | >200 |
| DMACB | 137.5 | 421 | 495 | — |
| NPRO | 74.0 | 434 | 459 | 17 |
| BNA | 64.4 | 495 | 378 | >108 |
| MNA | 50.6 | 498 | 406 | 13 |

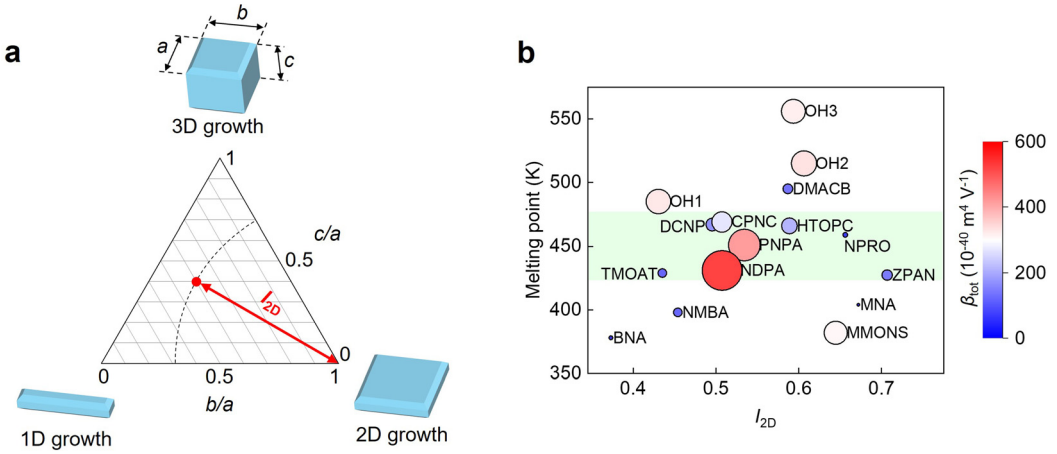


Fig. 1 Screening by crystal habit. (a) Definition of the crystal-habit parameter $l_{2D}$ in a triangle graph as a function of growth anisotropies (see text). $l_{2D}$ corresponds to the distance from the 2D crystal growth in the triangle graph. (b) Plot of the melting point $T_m$ of EO molecular crystals as a function of $l_{2D}$. The size and color gradation of the symbols represent the magnitude of total hyperpolarizability (non-resonant) $\beta_{tot}$ (see text). The green shaded zone indicates the temperature range suitable for the optoelectronic integration by melt casting (see text).

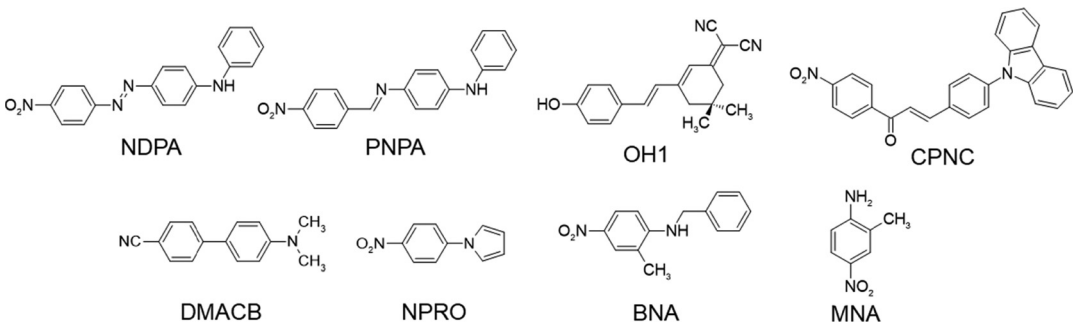


Fig. 2 EO molecular crystals with 2D crystal growth. Molecular structures of the EO molecular crystals investigated in this study.

in terms of film formability. On the other hand, regarding the melting point, the moderate $T_m$ ranging approximately from 420 to 480 K is favorable as indicated by the shaded zone in Fig. 1b, because the lower $T_m$ causes thermal instability and the higher $T_m$ reduces the processability, especially for melt casting. Thus, NDPA, PNPA, OH1, and (*E*)-3-(4-carbazol-9-ylphenyl)-1-(4-nitrophenyl)prop-2-en-1-one (CPNC), which satisfy the criteria of $\beta_{tot} > 200 \times 10^{-40}$ m$^4$ V$^{-1}$, $l_{2D} < 0.6$, and $T_m \sim 450$ K, were extracted as the EO molecular crystals with high EO activity, film formability, and thermal stability (see Fig. 2 and Table 1).

### 2.2 Film-formability test by melt casting

Film formability of the EO molecular crystals extracted *via* materials screening were experimentally examined by melt casting. For comparison, the experiments were also conducted for BNA, 4-*N*,*N*-dimethylamino-4′-cyanobiphenyl (DMACB), 1-(4-nitrophenyl)-1*H*-pyrrole (NPRO), and 2-methyl-4-nitroaniline (MNA) which do not satisfy one or more of the screening criteria for $l_{2D}$, $\beta_{tot}$, and $T_m$ mentioned in Section 2.1. As shown in Fig. 3a, the powder samples sandwiched by the upper and lower substrates were heated above $T_m$ so as to melt and spread along the gap between the two substrates due to capillary action. After cooling slowly, they solidified to form thin films. In this study, solution-based processes such as spin coating were not employed because they often cause inhomogeneity in crystal orientation due to non-uniform solvent evaporation, resulting in the formation of small crystallites and polycrystalline domains. Fig. 3b shows the result of melt casting. The crystallite size increased as the order of NPRO (<50 μm) < MNA (<200 μm) < DMACB (>1000 μm) < PNPA (>1000 μm) < NDPA (>1000 μm), which roughly obeyed the decrease of $l_{2D}$: MNA (0.67) > NPRO (0.66) > DMACB (0.59) > PNPA (0.53) > NDPA (0.51). However, it decreased in CPNC (<50 μm), OH1 (<1 μm), and BNA (<50 μm) despite small $l_{2D}$: CPNC (0.51), OH1 (0.43), and BNA (0.37). This deviation can be ascribed to super cooling. As shown in Table 1 and Fig. S2c, d, h, these materials exhibited noticeable supercooling ($T_m - T_s > 100$ K), which interfered crystal growth due to abrupt crystallization. It should be noted that DMACB solidified to an EO-inactive polymorph through the melt casting, as confirmed by DSC and SHG experiments (see SI and Fig. S2f). The remainder PNPA and NDPA, whose melting points and crystal habit predictions are in the preferable range, do not suffer from neither undesired supercooling nor polymorphism. Consequently, these two EO molecular crystals afforded to form single crystal films with the size of >1000 μm easily. Note that they are reported to be isostructural[34–36] and gave

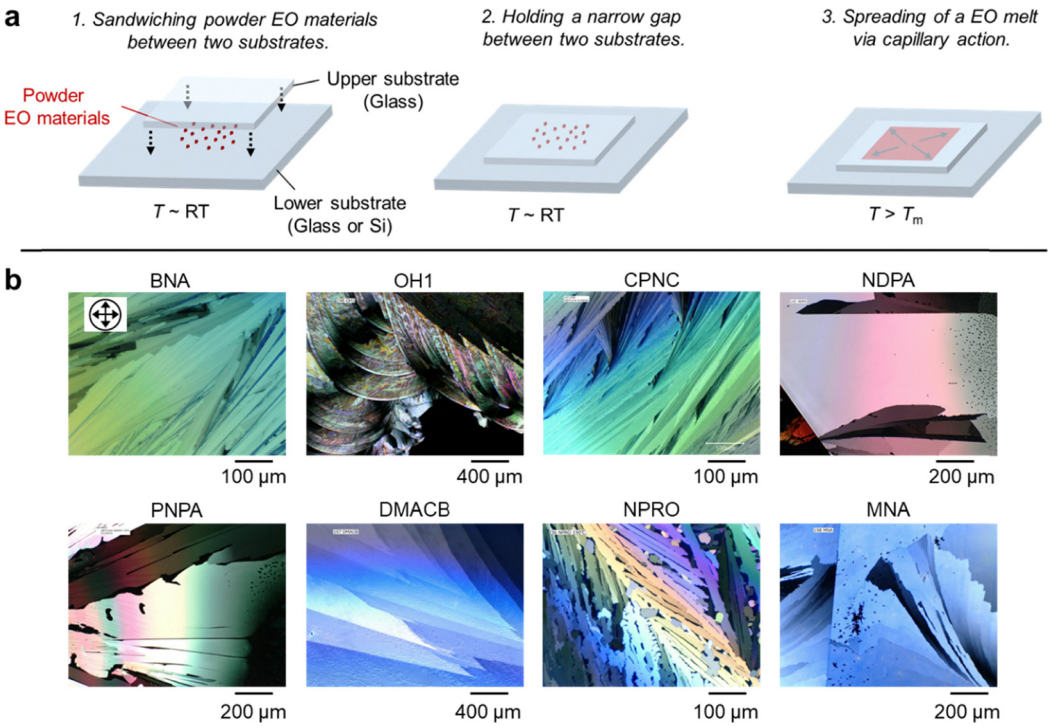


Fig. 3 Thin-film growth by melt-casting process. (a) Schematics of thin-film fabrication by melt-casting process. (b) Crossed-Nicols images for thin films of EO molecular crystals fabricated by this process.

almost isomorphous film morphologies; these films were confirmed to possess the in-plane polar axis, which is parallel to the [102] direction within the (010) plane (SI). This feature is suitable for the application of EO modulator, especially in the slot waveguide configuration.

To demonstrate the potential for integration with optoelectronic device, the fabrication of thin films within ultra-narrow silicon slots mimicking slot waveguides (the typical slot width of 100–200 nm) by the melt casting was examined for PNPA. We prepared the silicon substrate with rectangular sub-micron-width slots by lithography. Fig. 4a and b show the polarized and crossed-Nicols images of the resulting films within the silicon slots. For the 2 μm-wide slot, it appears to be homogeneously colored in the crossed-Nicols image due to the birefringence of EO material, clearly indicating the successful filling of not polycrystalline but single-crystalline PNPA films. However, for slots narrower than 190 nm, it is difficult to determine from optical microscopy whether the EO material is fully filled. Thus, we conducted atomic force microscope (AFM) and scanning electron microscope (SEM) measurements to directly evaluate the fillings. For AFM, we selectively measured regions within the 190 nm-wide slot where the filling appeared to be partially interrupted (see Fig. 4a). The depth profiles clearly distinguish between filled and unfilled regions (see Fig. 4c and d); the unfilled regions exhibit a depth of $>150$ nm (the present slot depth $\sim 250$ nm), whereas the filled regions show no height difference relative to the surrounding silicon surface. This confirms that PNPA fully occupies the sub-micron-width slot volume. Cross-sectional SEM image also reveals the filling of the slot for 190 nm by PNPA (Fig. 4e); it can be clearly observed that PNPA selectively flows into only the slot region.

Furthermore, to more rigorously validate the compatibility of PNPA with practical device structures, we fabricated a silicon slot-waveguide structure on silicon-on-insulator (SOI) substrate, incorporating metal electrodes on both sides of the slot (see Fig. S5, S6 and Section 4). Following the formation of the silicon rib waveguide, a central slot (100 nm wide and 220 nm deep) was introduced by electron-beam lithography. The etched slot fully penetrates the silicon waveguide and reaches the buried $SiO_2$ (BOX) layer (Fig. 4f). As shown in Fig. 4g and h, PNPA flows into the slot by the melt-casting process as well, producing a brightly colored crossed-Nicols image that indicates the formation of a high-quality crystalline film. These observations demonstrate that PNPA can be deposited even into device-level slot structures, highlighting its strong potential for integration into actual optoelectronic devices.

### 2.3 EO measurements

Let us uncover the EO performance of PNPA and NDPA thin films. Recently, the bulk crystal of PNPA was reported to show highly efficient terahertz wave generation.[34,37] Therefore, it is expected that PNPA and its isostructural material NDPA potentially demonstrate excellent EO performance in the thin film crystal forms as well. We employed the birefringence ferroelectric field-modulation imaging (FFMI)[38] for the EO evaluation. Applying the electric field to EO materials, the change in the refractive indexes through the EO effect yields the slight modulation of the birefringence of EO materials. This technique

 

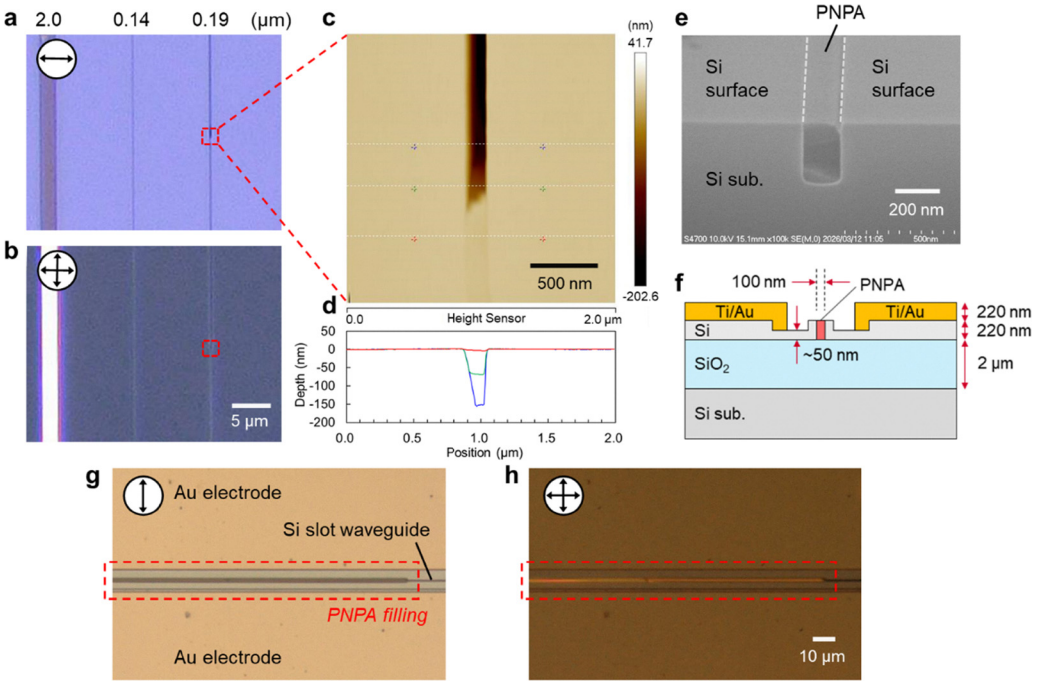


Fig. 4 Filling of thin films by melt-casting process. Polarized microscope image (a) and crossed-Nicols image (b) of PNPA films grown into narrow slots in the silicon substrate. Each slot width is indicated at the top. (c) AFM image of 190 nm slot in the silicon substrate. (d) Cross-sectional depth profiles extracted from the AFM topography shown in (c). (e) Cross-sectional SEM image of the 190 nm slot in the silicon substrate. (f) Schematic of the silicon slot-waveguide device structure. Polarized microscope image (g) and crossed-Nicols image (h) of PNPA films grown into narrow slots in the silicon slot waveguide on the SOI substrate.

detects it as the change in the transmitted light intensity $I_{\perp}$, $\Delta I_{\perp}$, by using a cross-polarized optical microscope (see Section 4 for details). We used a complementary metal–oxide–semiconductor (CMOS) image sensor as a detector (see Fig. S7), enabling spatially resolved measurements of EO performance over thin films.

To apply a transverse electric field to the EO films, interdigitated gold electrodes (line/space = 5/5 μm; DropSens, Spain) deposited on a glass substrate were used. We selected the domain whose polar axis is parallel to the electric field direction (surrounded by the dotted line in Fig. 5a) for measuring the EO performance. Fig. 5b and c show the crossed-Nicols ($I_{\perp}$) and modulation images ($\Delta I_{\perp}/I_{\perp}$) for PNPA obtained by FFMI at the wavelength of the incident light $\lambda$ = 810 nm. In the relevant region exhibiting the bright crossed-Nicols image due to the birefringence, the modulation signal was also clearly observed. This is reasonable because EO effect is maximized when the polar axis is parallel to the electric field. Note that the red and blue colors alternate in adjacent lines in Fig. 5c, meaning that the sign of $\Delta I_{\perp}/I_{\perp}$ is reversed (Fig. 5e) because of the electric field in the opposite direction on either side of the interdigitated electrodes (Fig. 5a). The modulation signal induced by the EO effect is much affected by the phase retardation of elliptically polarized outgoing light. In our measurements, we accurately controlled the phase retardation using the variable retarder set after the sample and measured $\Delta I_{\perp}/I_{\perp}$ under the various phase retardation values (see Fig. 5d and Section 4). From these measurements, the $n_3{}^3r_{33}$ values were evaluated to be ~1050 (1250) pm V$^{-1}$ for NDPA and ~690 (1200) pm V$^{-1}$ for PNPA at $\lambda$ = 810 (730) nm. Here, we set the directions parallel and perpendicular to the polar axis within the (010) plane (that is, the [102] and [$\bar{2}$0$\bar{1}$] directions, respectively) to the EO tensor indices 3 and 1. In these evaluations, other terms such as $r_{13}$ and $r_{53}$ are neglected because they are expected to be negligibly small relative to $r_{33}$ in the highly anisotropic crystal structure of NDPA and PNPA where the molecular hyper polarizability vectors align almost the same crystal direction. The enhancement of $n_3{}^3r_{33}$ at shorter wavelengths is due to the resonance effect near the absorption wavelength (corresponding to the intramolecular transition energy). We plotted the $n_3{}^3r_{33}$ values of NDPA and PNPA as a function of incident-light wavelength together with representative data for benchmark organic EO crystals (Fig. 6). Remarkably, the resulting wavelength dependence closely follows the EO performance of DAST and OH1, highlighting the excellent EO response of these materials. Moreover, we extrapolated the $n_3{}^3r_{33}$ values to the non-resonant telecommunications wavelength range using the widely adopted dispersion relation for EO performance,[39]

$$n^3 r = F\frac{\omega_0{}^2\left(3\omega_0{}^2 - \omega^2\right)}{\left(\omega_0{}^2 - \omega^2\right)^2}, \quad (1)$$

where $\omega_0$ is the resonance frequency and $F$ is the material parameter related to the molecular hyperpolarizability. The fitting well reproduces the measured $n_3{}^3r_{33}$ in the visible region. The extrapolated EO performance is about 500 pm V$^{-1}$ even at wavelengths far from resonance, which clearly surpasses that of LN ($n_3{}^3r_{33}$ ~ 320 pm V$^{-1}$). It is noteworthy that PNPA and NDPA

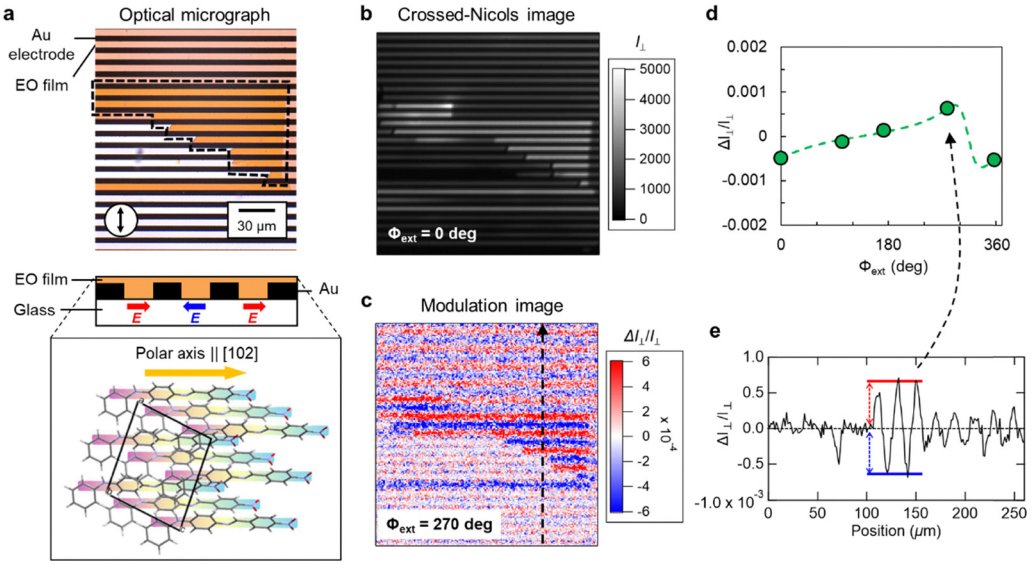


Fig. 5 Evaluation of the electro-optic performance for PNPA thin film at room temperature. (a) Polarized transmission micrograph of PNPA thin film on the glass substrate with interdigitated gold electrodes. The dark regions correspond to the electrodes. The orange-colored region surrounded by the dotted line corresponds to the domain where the polar axis (||[102]) is parallel to the electric field as shown in the lower panel (SI). The crystal structure of PNPA shown in the lower panel is viewed along the [010] direction. Crossed-Nicols (b) and modulation (c) images obtained by the FFMI measurements at $\lambda$ = 810 nm under $\phi_{ext}$ = 0 and 270 degrees, respectively. $\phi_{ext}$ is the phase retardation derived from the variable retarder (see text). (d) The $\phi_{ext}$ dependence of the modulation signal $\Delta I_\perp/I_\perp$ at $\lambda$ = 810 nm. (e) Cross-sectional plot of $\Delta I_\perp/I_\perp$ at the dashed arrow in the modulation image of (c).

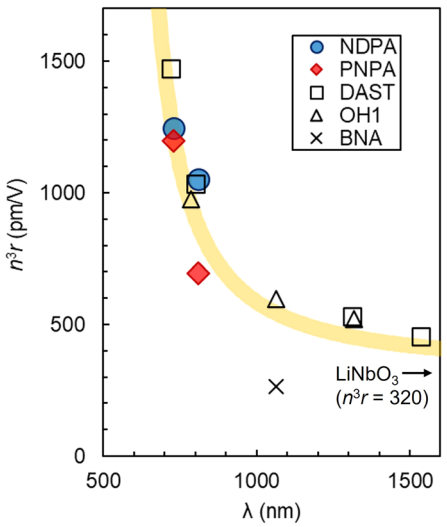


Fig. 6 Electro-optic performance in PNPA and NDPA thin films. The figure of merits for EO performance, $n_3{}^3r_{33}$, in PNPA and NDPA thin films evaluated by the FFMI measurements at room temperature. Reference data for benchmark EO crystals (DAST,[21] OH1,[22] and BNA[25,26]) are also plotted for comparison. The yellow curve represents the fit obtained using eqn (1) (see the main text), with the fitting parameters determined from the averaged $n_3{}^3r_{33}$ values of PNPA and NDPA.

not only exhibit high processability for thin film fabrication but also achieve excellent EO performance in the telecommunications bands.

### 2.4 Thermal stability test

We tested the thermal and long-term stabilities of EO performance for PNPA. Through the measurements at high temperatures up to 393 K, the $n_3{}^3r_{33}$ values of PNPA were confirmed to be temperature independent (Fig. 7a). The DSC analysis also indicated that PNPA exhibits only a peak by melting without any decomposition or phase transitions below $T_m$ = 452 K (Fig. 7b). Moreover, we conducted the accelerated aging test at 393 K in a nitrogen atmosphere. In Fig. 7c, we plotted the root mean square values of the modulation signals $\Delta I_\perp/I_\perp$, evaluated over the area of $>250 \times 250$ μm$^2$ in the PNPA film fabricated on the interdigitated electrode substrate, both with and without sealing using a glass plate (SI). Without sealing, $\Delta I_\perp/I_\perp$ degraded by 15% after 200 hours (Fig. 7c). This degradation was observed not only in the modulation image but also as a visible change in the optical microscope image (SI). In contrast, when sealed with a glass plate, $\Delta I_\perp/I_\perp$ showed almost no degradation (within 5%) even after 1000 hours. The strong suppression of degradation by sealing suggests that it is caused by local sublimation of the film surface rather than thermal decomposition. This outstanding thermal stability completely surpasses that of EO polymers, in which the EO performance degradation of 20–30% occurs at 393 K due to orientational relaxation of the aligned chromophores,[40] highlighting the significant advantage of crystalline EO materials. Compared to the widely accepted Telcordia GR-468-CORE standard (85 °C [= 358 K]/2000 hours) for optical device reliability,[41] the present evaluation was conducted at a higher temperature of 393 K, under which the EO performance remained stable for over 1000 hours. The ability to retain EO activity under such stringent conditions underscores the exceptional thermal stability of PNPA; notably, this material uniquely combines high EO performance, film formability, and long-term thermal stability, which is rarely achieved simultaneously in EO materials.

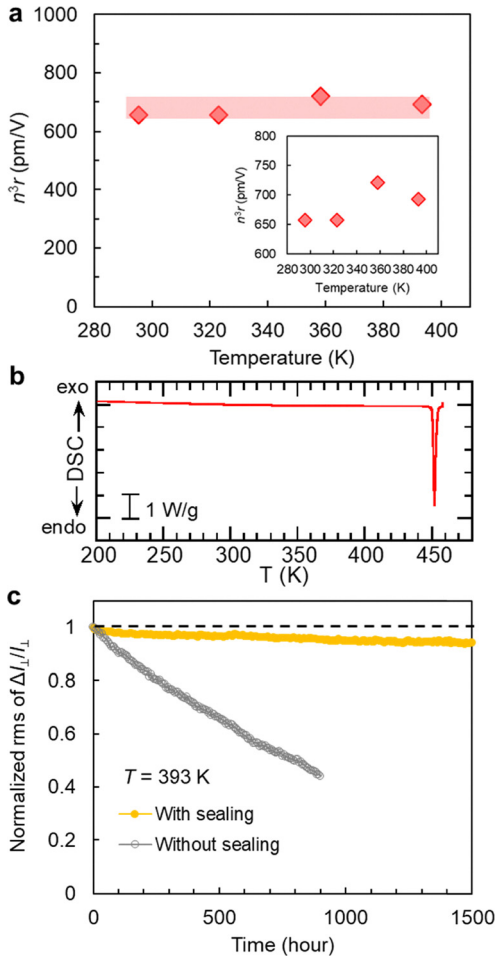


Fig. 7 Thermal stability for electro-optic performance in PNPA thin film. (a) Temperature dependence of the figure of merits for EO performance, $n_3^3r_{33}$, at $\lambda$ = 810 nm. The inset shows the expanded graph. (b) DSC measurement of PNPA (see SI). (c) Plot of the root mean square values of the modulation signal $\Delta I_\perp/I_\perp$ over the area of >250 × 250 μm$^2$ in the EO film fabricated on the interdigitated electrode substrate, measured at 393 K in a nitrogen atmosphere with and without sealing by the glass plate at $\lambda$ = 810 nm. The plotted values are normalized to the value at $t$ = 0 h.

### 2.5 Spontaneous ordering of crystal orientation by temperature gradient

To integrate an EO molecular crystal to an optical modulator with maximized EO efficiency, their crystal polar axis should be controlled to be parallel to applied electric field. On the other hand, the film orientation by the melt casting mentioned in Section 2.2 and 2.3 was random. Here, we demonstrate spontaneous ordering of crystal orientation by temperature gradient. A temperature gradient was generated between both ends of the substrate, with the low-temperature side set below $T_m$ and the high-temperature side above $T_m$. By lowering the temperature of the high-temperature side slowly, the thin film growth can be controlled to proceed along the temperature gradient where the nonmelted portion at the low-temperature side works as a seed crystal. Fig. 8a shows the crossed-Nicols micrograph of PNPA thin films fabricated under the temperature gradient using two different cooling rates for the high-temperature side: 30 K min$^{-1}$ (rapid cooling) at the upper half of the domains and 3 K min$^{-1}$ (slow cooling) at the lower half of the domains. A clearly oriented film along the temperature gradient was successfully obtained in the slow-cooled region. We show a histogram representing the distribution of domain orientation angles relative to the temperature gradient direction (Fig. 8b). It was revealed that the film in the rapid-cooled region exhibited random orientation, whereas the slow-cooled region showed distinct peaks in the domain distribution around 30° and −60°. These peak angles correspond to the tilt of the polar axis (∥[102]) with respect to the film growth direction (∥[001]) in PNPA (SI). These results indicate that the desired crystal orientation for integration into optical modulators can be achieved by controlling both the direction and cooling rate of temperature gradient.

Compared to electric-field poling, the temperature-gradient orientation control offers a significant advantage for fabricating large-area oriented films. Even under the preliminary experimental condition, the longitudinal size of the domain with controlled alignment exceeds 3 mm as shown in Fig. 8a. In the case of fabricating a slot-waveguide modulator using PNPA, the device length required for π phase shift ($V_\pi L$) was estimated to be ~0.5 mm, based on the equation $V_\pi L = \lambda g/2n_3^3r_{33}\Gamma$,[42] which is well within the aligned domain fabricated in this study. This estimation assumed $n_3^3r_{33}$ = 700 pm V$^{-1}$, $\lambda$ = 810 nm, the applied voltage of 1 V, the electrode gap $g$ = 190 nm (corresponding to the narrowest slot width successfully filled with PNPA in this study (see Fig. 4c)), and the interaction factor between the electrical and optical electric field $\Gamma$ = 0.2, a typical value in silicon-organic hybrid modulators.[42] Further optimization of the temperature gradient and cooling conditions is expected to enable orientation control over larger areas, suggesting the high potential of this approach for large-scale integration in optoelectronic devices.

### 2.6 Material design of EO molecular crystals for optoelectronic integration

Finally, we discuss the exceptional performance of EO activity, thin-film formability, and thermal stability observed in PNPA and NDPA from a material design perspective. Both molecules are composed of strong donor (*N*-phenylamino) and acceptor (nitro) groups connected *via* an extended π-conjugated bond (benzylideneaniline for PNPA, azobenzene for NDPA) (see Fig. 2), which is responsible for the large calculated hyperpolarizability $\beta$ (Table 1). To efficiently translate microscopic $\beta$ into macroscopic EO coefficients within the crystalline lattice, the relative orientation $\theta$ between molecular hyperpolarizability vector and crystal polar axis is required to be close to zero because the diagonal component of EO tensor is proportional to $\cos^3\theta$. Remarkably, in both PNPA and NDPA, the molecular dipoles are nearly perfectly aligned along the polar axis [102] as shown in Fig. 5a (*e.g.* $\cos^3\theta$ ~ 0.9998 for PNPA[43]), so that the EO performance is significantly enhanced in crystals. By contrast, EO polymers rely on electric-field poling, and even under strong fields the EO chromophores typically reach orientational order parameter of only $\cos^3\theta$ = 0.2–0.4.[12] Consequently, the highly oriented molecular arrangements in PNPA and NDPA result in the comparable EO performance with EO polymers, even despite the somewhat smaller molecular $\beta$

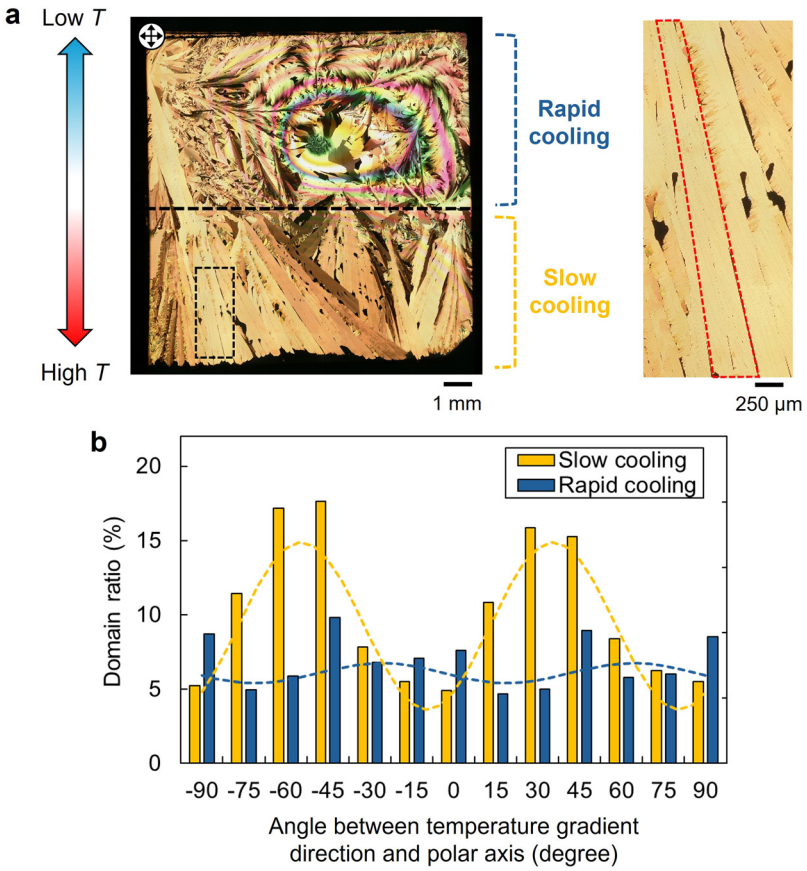


Fig. 8 Unidirectional crystal growth by temperature gradient in PNPA thin film. (a) Crossed-Nicols image of the PNPA film fabricated by the melt casting under the temperature gradient (see text). The dashed black rectangle represents the area shown in the enlarged image on the right. The dashed red box in the enlarged figure is guide for the oriented domain. (b) Distribution of domain orientation angles relative to the temperature gradient direction (see text).

values compared with high-performance EO chromophores. Such large π-conjugation typically leads to red-shifted absorption edges due to the reduction of the HOMO–LUMO gap; a clear trend can be observed among NDPA, PNPA, OH1 and CPNC with relatively similar molecular structures as seen in the $\lambda_{th}$ values summarized in Table 1. The red shift of the absorption edge yields enhanced EO activity due to the resonance effect close to the measurement wavelength. Regarding thermal stability, the extended π-conjugation also tends to correlate with the increased $T_m$, leading to their robust EO performance at elevated temperatures. Thin-film formability, in contrast, is not trivially linked to molecular structure. In this study, we adopted a crystal habit-based approach and selected the materials with 2D growth. Consequently, we successfully demonstrated high-quality film formation in PNPA and NDPA, suggesting the effectiveness of this approach. Thus, the combination of the molecular design for high EO response and the crystal habit prediction for 2D growth presents a promising pathway for the exploration of EO molecular crystals suitable for optoelectronic integration.

## 3 Conclusion

In summary, we explored the novel EO molecular crystals, NDPA and PNPA, that exhibit high EO performance with $n_3^3 r_{33}$ values exceeding ~700 pm $V^{-1}$ in the visible region, surpassing that of conventional material of LN. These materials also demonstrate excellent film formability and thermal stability up to 393 K, fulfilling the critical requirements for optoelectronic integration. The orientation control of thin film by temperature-gradient melt casting offers a scalable approach to achieving alignment without electric-field poling, enabling the convenient fabrication of uniformly aligned films over large areas. The excellent integration ability into narrow slot (*e.g.* 190 nm) further highlights the practical advantages of these materials for integrated slot waveguide devices. The present discovery was guided by materials screening strategy based on crystal habit prediction, where we focused on identifying molecules with high 2D crystal growth. Among them, we selected candidates with large $\beta$ and high $T_m$, enabling not only efficient EO response but also robust device operation under elevated temperatures. Historically, molecular crystals have been largely overlooked in the context of silicon photonics, mainly due to concerns about poor film formation. However, the successful fabrication of thin-films with high and thermally stable EO performance in PNPA and NDPA demonstrates the applicability of molecular crystals in silicon-organic hybrid photonic devices. This breakthrough suggests the potential to outperform polymer-based EO devices, especially in large-area applications under high thermal conditions. Thus, the present

findings address current limitations of existing EO materials and establish molecular crystals as compelling candidates for next-generation large-scale photonic technologies, including a high-speed optical modulator, an optical phased array, and a spatial light modulator.

# 4 Experimental section

## 4.1 General

PNPA and CPNC were prepared according to the reported procedure,[34,44] and NDPA (known also as the Disperse Orange 1 (DO1)) was purchased from Angene Co. Ltd. They were purified by repeating twice the vacuum sublimation under temperature gradient. The prismatic crystals of PNPA with well developed $(1\bar{1}0)$ planes were grown by slow evaporation of dichloromethane solution, whereas the brownish red elongated plates of NDPA crystals developed with the (010) planes were obtained during the sublimation process.

The other commercially available OH1 (TakachihoSangyo), DMACB (ChemCollect GmbH), BNA (Angene Co. Ltd), MNA and NPRO (Tokyo Chemical Industry) were purified by the vacuum sublimation under temperature gradient and recrystallization before use.

## 4.2 Diffuse reflectance spectra measurements

Diffuse reflectance spectra were measured using a Shimadzu UV-3150 spectrometer equipped with an integrating sphere accessory (Shimadzu ISR-3100) and transformed into absorption spectra by Kubelka–Munk function. The absorption threshold wavelength $\lambda_{th}$ was determined by linearly extrapolating the steep falloff region of the spectra on the long-wavelength side to zero intensity.

## 4.3 DSC measurements

The thermal analysis was performed using a differential scanning calorimeter (DSC7000X; Hitachi High-Technologies Corp., Tokyo). The sample was encapsulated in an aluminum pan and heated at a rate of 5 K $min^{-1}$. The temperature was calibrated by using the melting point of indium (429.8 K). The melting points determined by DSC agree with the reported maxima[34,45–50] within 3 K except for the CPNC without the reported data.

## 4.4 Calculation of hyperpolarizability

We calculated the hyperpolarizability $\beta$ by Gaussian 16 software.[51] In the previous quantum chemical calculations[34] using B3LYP DFT functional[52] and the 6-311++G basis set, the total hyperpolarizability $\beta_{tot}$ values at $\lambda = \infty$ ($\omega = 0$) were calculated to be 1321 $\times$ $10^{-40}$ (1070 $\times$ $10^{-40}$) $m^4$ $V^{-1}$ for a PNPA (NDPA) molecule. The re-examination in this study reproduced almost the same results [1406 $\times$ $10^{-40}$ (1057 $\times$ $10^{-40}$) $m^4$ $V^{-1}$] using the B3LYP/6-311++G(d,p). However, these calculations using the B3LYP functional do not include the long-range electron interaction properly and tend to overestimate the magnitude of $\beta$ with expanding the $\pi$-conjugated system as in the present case of PNPA and NDPA. Instead, recent theoretical simulations using the proper functionals demonstrate the improved agreements with experimental $\beta$ values.[53,54] Thus, we recalculated the $\beta$ using the long-range corrected functional such as the CAM-B3LYP/6-311++G(d,p)[55] as recommended. The revised $\beta_{tot}$ $(-\omega;\ \omega,\ 0)$ values of PNPA (NDPA) are 416.8 $\times$ $10^{-40}$ (521.2 $\times$ $10^{-40}$) $m^4$ $V^{-1}$ at $\lambda = \infty$ ($\omega = 0$), 702.7 $\times$ $10^{-40}$ (862.8 $\times$ $10^{-40}$) $m^4$ $V^{-1}$ at $\lambda$ = 810 nm, and 808.4 $\times$ $10^{-40}$ (989.0 $\times$ $10^{-40}$) $m^4$ $V^{-1}$ at $\lambda$ = 730 nm. It should be also noted that the order of magnitude in the two isomorphous materials is reversed to NDPA > PNPA. This relationship is verified by the EO performance (see Section 2.3), suggesting the importance of the long-range corrections in the cases of PNPA and NDPA. For other organic materials listed in Fig. 1, we calculated the $\beta_{tot}$ $(-\omega;\ \omega,\ 0)$ values using the similar functional of CAM-B3LYP/6-311++G(d,p).

The $\beta_{tot}$ values listed in Table 1 are given in SI units, and the conversion between cgs and SI units is 1 $\times$ $10^{-30}$ esu = 4.18 $\times$ $10^{-40}$ $m^4$ $V^{-1}$.

## 4.5 Atomic force microscopy (AFM) measurement

AFM measurements were performed using a commercial Dimension 3000/Nanoscope IIIa system (Bruker, USA) in tapping mode under ambient conditions.

## 4.6 Scanning electron microscope (SEM) measurement

SEM measurements were performed using a commercial S-4700 system (HITACHI, Japan). The observation target was coated with a thin ($\sim$5 nm) layer of platinum to prevent charging.

## 4.7 Fabrication of silicon slot waveguide structure

Silicon slot waveguides were fabricated on an SOI substrate with top Si and buried-oxide layer thicknesses of 220 nm and 2 μm, respectively. First, the substrate was cleaned using a wet process. Next, the rib waveguide was patterned using an electron beam lithography (EBL) system (Elionix, Japan) with an acceleration voltage of 130 kV and a beam current of 1.5 nA. The Si layer was then shallowly etched using an inductively coupled plasma reactive ion etching (ICP-RIE) system (SPP Technologies, Japan) with $C_4F_8$ and $SF_6$ gases, leaving approximately 50 nm of the Si layer. Subsequently, the slot gap was formed using the same procedure, with alignment performed using metal marks on the device chip, and the slot was completely etched down to the $SiO_2$ layer. Finally, electrodes consisting of titanium and gold layers with a total thickness of 220 nm were formed by a lift-off process, completing the slot waveguide structure.

## 4.8 Birefringence FFMI measurement

We employed the birefringence FFMI technique to evaluate the EO performance (see Fig. S7 for the detailed setup[38]). When the polar axis of the EO film is set to the direction tilted 45° from the polarizer in the crossed-Nicols configuration, the intensity of transmitted light $I_\perp$ is expressed as

$$I_\perp = I_{\perp 0} + I_{\perp 1} \sin^2\left(\frac{\phi_0}{2}\right), \quad (2)$$

where $\phi_0$ is the phase retardation between the components of elliptically polarized outgoing light along the directions parallel and perpendicular to the polarizer. It is expressed as $\phi_0 = \frac{2\pi d}{\lambda} n_{\mathrm{aniso}}$ ($n_{\mathrm{aniso}} = n_3 - n_1$) with the refractive index along the direction parallel (perpendicular) to the polar axis within the (010) plane, $n_{3(1)}$. The point group of PNPA and NDPA is $m$,[34–36] for which the related EO tensors are $r_{33}$, $r_{13}$, and $r_{53}$ when the electric field along the polar axis ($\|3$) $E_3$ is applied. The terms of $r_{13}$ and $r_{53}$ are expected to be negligibly small relative to $r_{33}$ because the present systems are highly one-dimensional. Thus, we assume that the change in the anisotropy of the refractive indexes through the EO effect is described as $\Delta n_{\mathrm{aniso}} = -\frac{1}{2} n_3^3 r_{33} E_3$. This leads to the modulation of the outgoing light intensity, $\Delta I_\perp$, as follows,

$$\Delta I_\perp = I_{\perp 1}\left[\sin^2\left(\frac{\phi_0}{2} + \frac{\pi d}{\lambda}\Delta n_{\mathrm{aniso}}\right) - \sin^2\left(\frac{\phi_0}{2} - \frac{\pi d}{\lambda}\Delta n_{\mathrm{aniso}}\right)\right]. \quad (3)$$

To sensitively detect the modulation signals, we used the variable retarder as described in Section 2.3. In this case, $\phi_0$ in eqn (2) and (3) is replaced with $\phi_0 + \phi_{\mathrm{ext}}$, where $\phi_{\mathrm{ext}}$ is the controllable phase retardation ($0 \leqq \phi_{\mathrm{ext}} < 2\pi$) derived from the birefringence of the variable retarder. The slow axis of the variable retarder is parallel to the polar axis of the EO thin film. By fitting of eqn (2) and (3) to $I_\perp$ and $\Delta I_\perp / I_\perp$ measured under the various $\phi_{\mathrm{ext}}$ values, $\Delta n_{\mathrm{aniso}}\left(= -\frac{1}{2} n_3^3 r_{33} E_3\right)$ can be obtained.

In the present study, the applied ac voltage was $\pm 2$ V with the modulation frequency of 45 Hz. The gap between the electrodes was 5 μm. The thin-film thickness of PNPA (NDPA) used in the birefringence FFMI measurement was 130 nm (1.2 μm), which was determined by AFM.

## Author contributions

K. S. performed investigation, analysis, and funding acquisition, and wrote the original draft. S. H. performed conceptualization, investigation, analysis, review and editing. Y. S. performed investigation, analysis, review and editing. N. F. performed investigation. T. H. performed calculations for molecules, funding acquisition, review and editing. Y. A. provided resources and performed review and editing. S. I. performed preliminary calculations for crystals, review and editing. J. T. performed conceptualization, supervision, analysis, funding acquisition, review and editing. All authors have read and agreed to the final version of the manuscript.

## Conflicts of interest

There are no conflicts to declare.

## Data availability

The data supporting this article have been included as part of the supplementary information (SI). Supplementary information is available. See DOI: https://doi.org/10.1039/d6mh00613b.

## Acknowledgements

The authors thank A. Otomo (National Institute of Information and Communications Technology) for fruitful discussion. This work was supported by the JSPS Grants-in-Aid for Scientific Research (Grant No. 24K17021, 25H00836, and 25H01405). Part of the computation was performed using Research Center for Computational Science, Okazaki, Japan (Project: 24-IMS-C321).

## References

1 M. Abarkan, J. P. Salvestrini, M. D. Fontana and M. Aillerie, *Appl. Phys. B*, 2003, **76**, 765–769.
2 N. Margalit, C. Xiang, S. M. Bowers, A. Bjorlin, R. Blum and J. E. Bowers, *Appl. Phys. Lett.*, 2021, **118**, 220501.
3 S. Shekhar, W. Bogaerts, L. Chrostowski, J. E. Bowers, M. Hochberg, R. Soref and B. J. Shastri, *Nat. Commun.*, 2024, **15**, 751.
4 S. Y. Siew, B. Li, F. Gao, H. Y. Zheng, W. Zhang, P. Guo, S. W. Xie, A. Song, B. Dong, L. W. Luo, C. Li, X. Luo and G. Q. Lo, *J. Lightwave Technol.*, 2021, **39**, 4374–4389.
5 A. Rahim, T. Spuesens, R. Baets and W. Bogaerts, *Proc. IEEE*, 2018, **106**, 2313–2330.
6 G. T. Reed, G. Z. Mashanovich, F. Y. Gardes, M. Nedeljkovic, Y. Hu, D. J. Thomson, K. Li, P. R. Wilson, S. W. Chen and S. S. Hsu, *Nanophotonics*, 2014, **3**, 229–245.
7 A. Liu, L. Liao, D. Rubin, H. Nguyen, B. Ciftcioglu, Y. Chetrit, N. Izhaky and M. Paniccia, *Opt. Express*, 2007, **15**, 660–668.
8 M. He, M. Xu, Y. Ren, J. Jian, Z. Ruan, Y. Xu, S. Gao, S. Sun, X. Wen, L. Zhou, L. Liu, C. Guo, H. Chen, S. Yu, L. Liu and X. Cai, *Nat. Photonics*, 2019, **13**, 359–364.
9 I. Taghavi, M. Moridsadat, A. Tofini, S. Raza, N. A. F. Jaeger, L. Chrostowski, B. J. Shastri and S. Shekhar, *Nanophotonics*, 2022, **11**, 3855–3871.
10 C. Wang, M. Zhang, X. Chen, M. Bertrand, A. Shams-Ansari, S. Chandrasekhar, P. Winzer and M. Lončar, *Nature*, 2018, **562**, 101–104.
11 Y. Shi, C. Zhang, H. Zhang, J. H. Bechtel, L. R. Dalton, B. H. Robinson and W. H. Steier, *Science*, 2000, **288**, 119–122.
12 L. R. Dalton, P. A. Sullivan and D. H. Bale, *Chem. Rev.*, 2010, **110**, 25–55.
13 S. I. Inoue and A. Otomo, *Appl. Phys. Lett.*, 2013, **103**, 171101.
14 H. Xu, D. L. Elder, L. E. Johnson, Y. de Coene, S. R. Hammond, W. Vander Ghinst, K. Clays, L. R. Dalton and B. H. Robinson, *Adv. Mater.*, 2021, **33**, 2104174.

 

15 D. L. Elder and L. R. Dalton, *Ind. Eng. Chem. Res.*, 2022, **61**, 1207–1231.
16 V. R. Almeida, Q. Xu, C. A. Barrios and M. Lipson, *Opt. Lett.*, 2004, **29**, 1209–1211.
17 H. Xu, F. Liu, D. L. Elder, L. E. Johnson, Y. De Coene, K. Clays, B. H. Robinson and L. R. Dalton, *Chem. Mater.*, 2020, **32**, 1408–1421.
18 G. W. Lu, J. Hong, F. Qiu, A. M. Spring, T. Kashino, J. Oshima, M. Ozawa, H. Nawata and S. Yokoyama, *Nat. Commun.*, 2020, **11**, 4224.
19 H. Nakanishi, H. Matsuda, S. Okada and M. Kato, *Proc. MRS Int. Meet. Adv. Mater.*, 1989, **1**, 97–104.
20 S. R. Marder, J. W. Perry and W. P. Schaefer, *Science*, 1989, **245**, 626–628.
21 F. Pan, G. Knöpfle, C. Bosshard, S. Follonier, R. Spreiter, M. S. Wong and P. Günter, *Appl. Phys. Lett.*, 1996, **69**, 13–15.
22 C. Hunziker, S.-J. Kwon, H. Figi, F. Juvalta, O.-P. Kwon, M. Jazbinsek and P. Günter, *J. Opt. Soc. Am. B*, 2008, **25**, 1678–1683.
23 O. P. Kwon, S. J. Kwon, M. Jazbinsek, F. D. J. Brunner, J. I. Seo, C. Hunziker, A. Schneider, H. Yun, Y. S. Lee and P. Günter, *Adv. Funct. Mater.*, 2008, **18**, 3242–3250.
24 M. Jazbinsek, U. Puc, A. Abina and A. Zidansek, *Appl. Sci.*, 2019, **9**, 882.
25 M. Fujiwara, M. Maruyama, M. Sugisaki, H. Takahashi, S. Aoshima, R. J. Cogdell and H. Hashimoto, *Jpn. J. Appl. Phys.*, 2007, **46**, 1528–1530.
26 W. Sun, Z. Wang, A. Chen, I. Kosilkin, D. Bale and L. R. Dalton, *Opt. Express*, 2011, **19**, 11189–11195.
27 D. Korn, M. Jazbinsek, R. Palmer, M. Baier, L. Alloatti, H. Yu, W. Bogaerts, G. Lepage, P. Verheyen, P. Absil, P. Guenter, C. Koos, W. Freude and J. Leuthold, *IEEE Photonics J.*, 2014, **6**, 2700109.
28 D. R. Kanis, M. A. Ratner and T. J. Marks, *Chem. Rev.*, 1994, **94**, 195–242.
29 J. Liu, C. Ouyang, F. Huo, W. He and A. Cao, *Dyes Pigm.*, 2020, **181**, 108509.
30 G. Clydesdale, R. Docherty and K. J. Roberts, *Comput. Phys. Commun.*, 1991, **64**, 311–328.
31 G. Clydesdale, K. J. Roberts and R. Docherty, *J. Cryst. Growth*, 1996, **166**, 78–83.
32 A. Gavezzotti, *Acc. Chem. Res.*, 1994, **27**, 309–314.
33 A. Gavezzotti and G. Filippini, *J. Phys. Chem.*, 1994, **98**, 4831–4837.
34 G. A. Valdivia-Berroeta, Z. B. Zaccardi, S. K. F. Pettit, S. H. Ho, B. W. Palmer, M. J. Lutz, C. Rader, B. P. Hunter, N. K. Green, C. Barlow, C. Z. Wayment, D. J. Ludlow, P. Petersen, S. J. Smith, D. J. Michaelis and J. A. Johnson, *Adv. Mater.*, 2022, **34**, 2107900.
35 T. E. Souza, A. O. L. Iara Maria Landre Rosa, D. Paschoal, L. J. Q. Maia, H. F. Dos Santos, F. T. Matins and A. C. Doriguetto, *Acta Crystallogr., Sect. B: Struct. Sci., Cryst. Eng. Mater.*, 2015, **71**, 416–426.
36 O. S. Bushuyev, T. A. Singleton and C. J. Barrett, *Adv. Mater.*, 2013, **25**, 1796–1800.
37 C. Rader, Z. B. Zaccardi, S. H. E. Ho, K. G. Harrell, P. K. Petersen, M. F. Nielson, H. Stephan, N. K. Green, D. J. H. Ludlow, M. J. Lutz, S. J. Smith, D. J. Michaelis and J. A. Johnson, *ACS Photonics*, 2022, **9**, 3720–3726.
38 K. Sunami, S. Horiuchi, S. Ishibashi and J. Tsutsumi, *Adv. Electron. Mater.*, 2025, **11**, 2400346.
39 C. Bosshard, K. Sutter, R. Schlesser and P. Giinter, *J. Opt. Soc. Am. B*, 1993, **10**, 867–885.
40 A. Schwarzenberger, A. Mertens, H. Kholeif, A. Kotz, C. Eschenbaum, L. E. Johnson, D. L. Elder, S. R. Hammond, K. O'Malley, L. Dalton, S. Randel, W. Freude and C. Koos, *49th Eur. Conf. Opt. Commun. (ECOC 2023)*, 2023, **2023**, 859–862.
41 Telcordia, GR-468-CORE, 2004.
42 W. Freude, A. Kotz, H. Kholeif, A. Schwarzenberger, A. Kuzmin, C. Eschenbaum, A. Mertens, S. Sarwar, P. Erk, S. Brase and C. Koos, *IEEE J. Sel. Top. Quantum Electron.*, 2024, **30**, 3400222.
43 K. M. Holland, A. Alejandro, D. J. H. Ludlow, P. K. Petersen, M. A. Wright, C. C. Chartrand, D. J. Michaelis, J. A. Johnson and J. E. Patterson, *Opt. Lett.*, 2023, **48**, 5855–5858.
44 M. F. Zaini, I. A. Razak, W. M. Khairul and S. Arshad, *Acta Crystallogr., Sect. E: Crystallogr. Commun.*, 2020, **76**, 387–391.
45 S. Makita, A. Saito, M. Hayashi, S. Yamada, K. Yoda, J. Otsuki, T. Takido and M. Seno, *Bull. Chem. Soc. Jpn.*, 2000, **73**, 1525–1533.
46 H. Hashimoto, Y. Okada, H. Fujimura, M. Morioka, O. Sugihara, N. Okamoto and R. Matsushima, *Jpn. J. Appl. Phys.*, 1997, **36**, 6754–6760.
47 X. Zhang, X. Jiang, Y. Li, Z. Lin, G. Zhang and Y. Wu, *CrystEngComm*, 2015, **17**, 1050–1055.
48 O. Vakuliuk, B. Koszarna and D. T. Gryko, *Adv. Synth. Catal.*, 2011, **353**, 925–930.
49 B. Zuo, J. Chen, M. Liu, J. Ding, H. Wu and W. Su, *J. Chem. Res.*, 2009, **2009**, 14–16.
50 M. Lemaire, A. Guy, P. Boutin and J. P. Guette, *Synthesis*, 1989, **10**, 761–763.
51 M. J. Frisch, G. W. Trucks, H. B. Schlegel, G. E. Scuseria, M. A. Robb, J. R. Cheeseman, G. Scalmani, V. Barone, G. A. Petersson, H. Nakatsuji, X. Li, M. Caricato, A. V. Marenich, J. Bloino, B. G. Janesko, R. Gomperts, B. Mennucci, H. P. Hratchian, J. V. Ortiz, A. F. Izmaylov, J. L. Sonnenberg, D. Williams-Young, F. Ding, F. Lipparini, F. Egidi, J. Goings, B. Peng, A. Petrone, T. Henderson, D. Ranasinghe, V. G. Zakrzewski, J. Gao, N. Rega, G. Zheng, W. Liang, M. Hada, M. Ehara, K. Toyota, R. Fukuda, J. Hasegawa, M. Ishida, T. Nakajima, Y. Honda, O. Kitao, H. Nakai, T. Vreven, K. Throssell, J. A. Montgomery, Jr., J. E. Peralta, F. Ogliaro, M. J. Bearpark, J. J. Heyd, E. N. Brothers, K. N. Kudin, V. N. Staroverov, T. A. Keith, R. Kobayashi, J. Normand,

K. Raghavachari, A. P. Rendell, J. C. Burant, S. S. Iyengar, J. Tomasi, M. Cossi, J. M. Millam, M. Klene, C. Adamo, R. Cammi, J. W. Ochterski, R. L. Martin, K. Morokuma, O. Farkas, J. B. Foresman and D. J. Fox, *Gaussian 16, Revision C.02*, Gaussian, Inc., Wallingford CT, 2019.

52 A. D. Becke, *J. Chem. Phys.*, 1993, **98**, 5648–5652.

53 L. E. Johnson, L. R. Dalton and B. H. Robinson, *Acc. Chem. Res.*, 2014, **47**, 3258–3265.

54 F. A. Santos, C. E. R. Cardoso, J. J. Rodrigues, L. De Boni and L. M. G. Abegão, *Photonics*, 2023, **10**, 545.

55 T. Yanai, D. P. Tew and N. C. Handy, *Chem. Phys. Lett.*, 2004, **393**, 51–57.